

Discovery of a mid-infrared protostellar outburst of exceptional amplitude

P. W. Lucas¹★, J. Elias, S. Points, Z. Guo¹, L.C. Smith², C. Morris¹, J. Borissova^{3,4}, R. Kurtev^{3,4}, C. Contreras Peña⁵, Nicolás Medina Peña³, D. Minniti^{3,6,7}, V.D. Ivanov⁸, R.K. Saito⁹

¹Royal Astronomical Society, Burlington House, Piccadilly, London W1J 0BQ, UK

²Department, Institution, Street Address, City Postal Code, Country

³Another Department, Different Institution, Street Address, City Postal Code, Country

Accepted XXX. Received YYY; in original form ZZZ

ABSTRACT

We report the discovery of a mid-infrared outburst in a Young Stellar Object (YSO) with an amplitude of 8 mag at $\lambda \approx 4.6 \mu\text{m}$. WISEA J142238.82-611553.7 is one of 23 highly variable WISE sources discovered in a search of Infrared Dark Clouds (IRDCs). It is located in the small IRDC G313.671-0.309 ($d \approx 2.6$ kpc), seen by the *Herschel*/HiGal survey as a compact, massive cloud core that may have been measurably warmed by the event. Pre-outburst data from GLIMPSE in 2004 suggest that it is a class I system, a view supported by detection of weak H_2 emission at $2.12 \mu\text{m}$ in an otherwise featureless red continuum spectrum taken in 2019 (6 mag below the peak in K_s). MIPS GAL, WISE and VVV data indicate that the outburst had begun by 2006, had a total duration > 13 yr and a relatively flat peak from 2010–2014. The low pre-outburst luminosity indicates a low mass progenitor, whilst the outburst luminosity of a few $\times 10^2 L_\odot$ is consistent with an accretion rate $\dot{M} \sim 10^{-4} M_\odot \text{yr}^{-1}$, comparable to a classical FU Orionis event. However, the $4.6 \mu\text{m}$ peak corresponds to $T \approx 800$ K and implies a disc radial location $r \geq 4.6$ au for the site of the burst. The unprecedented amplitude, the long duration and the SED peak at $4.6 \mu\text{m}$ place constraints on physical mechanisms, disfavoured the thermal instability theory and magnetic gating theories but perhaps consistent with the concept of gravitational instability in the outer disc and the infall of disc fragments.

Key words: keyword1 – keyword2 – keyword3

1 INTRODUCTION

Eruptive variable YSOs are YSOs wherein a sudden dramatic increase in the accretion rate causes a large increase in flux, with a duration ranging from a few months up to a century (Herbig 1977, 1989; Hartmann & Kenyon 1996; Audard et al. 2014; Contreras Peña et al. 2017). The prototypical outburst was that of FU Ori (Herbig 1977) with a rise of 6 mag in the visible, thought to be associated with a thousand-fold increase in accretion rate (REF), for reasons not yet established. For a long time, this was the largest photometric outburst known but optical variations of 7 mag were seen in the atypical “hot FUor” PTF14jg (Hillenbrand et al. 2019), where an initial 1 mag dip was followed by a 7 mag rise over 150 days. Detection of such very high amplitude events should make it possible to rule out some of the

physical mechanisms that have been proposed to explain them. There may however be more than one such mechanism, leading to events with different amplitudes and durations.

Traditionally, most high amplitude outbursts were detected in visible light but there has been a recent trend towards detection of events in YSOs at earlier stages of evolution, in the near infrared (Contreras Peña et al. 2017), in the submm and mm continuum (Safron et al. 2015; Hunter et al. 2017) and via methanol maser emission (Caratti o Garatti et al. 2016).

In this paper we report the mid-infrared detection of a YSO outburst with a rise of ~ 8 mag, higher than any previously known. This was a somewhat serendipitous discovery using data from the *WISE* satellite (Wright et al. 2010) (with pre-outburst data from the *Spitzer*/GLIMPSE survey (Benjamin et al. 2003)). It arose from an investigation of an exceptionally red transient in an infrared dark cloud (IRDC)

★ E-mail: p.w.lucas@herts.ac.uk (PWL)

(Lucas et al. 2020), wherein we constructed a WISE variability catalogue for sources in the environs of IRDCs in an attempt to detect additional examples of similar transients. While the mid-infrared waveband was used in the YSOVAR project to investigate the low amplitude YSO variability on relatively short timescales, this is the first outburst to be detected in this waveband. Several additional highly variable YSOs and other variable stars were detected as part of the same search, indicating that the ongoing WISE/Neowise mission is a valuable resource for exploring the mid-infrared variable sky in an unbiased manner.

In section 2 we describe our search for highly variable sources in the WISE data and briefly summarise the 23 sources found. In section 3 we present details of the extreme outbursting YSO, including multi-wavelength public survey data and follow-up spectroscopy. We then discuss what we can learn from the event in section 4, before summarising our conclusions in section 5.

2 VARIABLE STAR SEARCH

2.1 Method

We searched the WISE multi-epoch photometric catalogues for highly variable sources and transients projected within two arcminutes of any of the 7139 IRDCs in the list of Peretto et al. (2016) that were identified as bona fide dense molecular clouds in that work. These IRDCs showed evidence for 250 μm emission in an automated analysis of images from the Herschel/HiGal survey (Molinari et al. 2010). All the IRDCs are located in the *Spitzer*/GLIMPSE fields at Galactic latitudes $|b| < 1$ and longitudes $295 < l < 350^\circ$ or $10 < l < 65^\circ$.

The search was undertaken during an investigation of the bright and very red transient, VVV-WIT-01, which was projected against an IRDC from the list of Peretto & Fuller (2009). The covering fraction of IRDCs in the GLIMPSE region is only 1–2% (depending on whether unconfirmed IRDCs are included) so it was thought that this might be a pre-main sequence event. A search for additional transients in IRDCs therefore seemed logical, also offering the chance to detect eruptive YSOs and other high amplitude Galactic variable stars. It would be preferable to search the available WISE datasets more fully (e.g. using the unWISE images, Meisner et al. (2019)) but this would be a computationally demanding task. The two arcminute search radius was chosen because it provides high completeness for any sources inside IRDCs (98% of the 7139 confirmed IRDCs have a smaller equivalent radius). There are typically many WISE sources within a two arcminute radius in the Galactic plane, even at the depth of individual WISE scans. Each field of this size can include multiple YSOs (see e.g. Lucas et al. (2017)). The total area searched is approximately 2 deg², corresponding to 1% of the GLIMPSE area.

To construct a time domain catalogue in the WISE W1 (3.3 μm) and W2 (4.6 μm) passbands, we downloaded from IPAC/IRSA all catalogue entries in the WISE All-Sky Single Exposure (L1b) Source Table located within the 7139 areas. We performed similar downloads from the WISE 3-Band Cryo Single Exposure (L1b) Source Table, the WISE Post-Cryo Single Exposure (L1b) Source Table

and the NEOWISE-R Single Exposure (L1b) Source Table. Together these comprise data taken throughout 2010 and in the period from 2013 December to 2017 December. Since the WISE satellite scans the full sky every six months, the areas investigated typically have 10 epochs of observation. Each epoch is subdivided into several individual scans made over a ~ 1 day interval, for which photometry is recorded separately in the L1b source tables listed above.

We used the STILTS software to match the catalogue entries, grouping them into time sequences for individual sources with a matching radius of 2'' (about a third of the WISE beam width). Duplicates of catalogue entries that were associated with multiple adjacent IRDCs were removed. The per-scan magnitudes for detections in the W1 and W2 passbands and all the other associated catalogue parameters were then averaged to give values for each epoch. Starting with these epoch-averaged data for the 4-year NEOWISE-R dataset, the sources associated with each IRDC were then matched against the epoch-averaged data for the same IRDC drawn from the three WISE datasets that cover calendar year 2010. This provided a reasonably complete time domain catalogue for variable stars. To be as complete as possible for transients and high amplitude variables, we repeated the process using each of the three 2010 WISE datasets in turn to provide the initial source list.

In total, the resulting time domain catalogue contains a little over half a million sources. We investigated only the most promising high amplitude candidates. To search for variable stars, we selected sources that varied by at least two magnitudes (maximum minus minimum) in at least one of the two passbands (W1 and W2). We further required the following criteria to be satisfied for parameters in the WISE L1b source tables $\overline{NB} < 1.1$ (i.e. the number of deblended sources contributing to the detection is < 1.1 , after averaging over all epochs) and the following conditions concerning at least one of the two passbands (W1 and W2),

$$w1mpro < 9 \text{ AND } w1snr > 5 \quad \text{at one or more epochs}$$

$$\text{mean}(w1chi) < 5 \text{ OR } \text{mean}(w1chi) < \frac{(\max(w1snr) - 3)}{7}$$

$$w2mpro < 9 \text{ AND } w2snr > 5 \quad \text{at one or more epochs}$$

$$\text{mean}(w2chi) < 5 \text{ OR } \text{mean}(w2chi) < (0.1 \max(w2snr) - 0.3)$$

Here $w1mpro$ and $w2mpro$ are the W1 and W2 magnitudes, snr refers to the signal to noise ratio in the indicated passband and chi refers to the χ parameter derived from comparison of the image profile with a point source model. The relations between the chi and snr parameters are those taken from Koenig & Leisawitz (2014). For each passband, the chi parameter was averaged over all epochs and the highest value of the snr parameter was used.

This selection yielded 177 candidates, all of which were visually inspected using the multi-epoch images of the individual scans available at IPAC/IRSA. Of these, 14 were confirmed as bona fide high amplitude variable stars. A further nine bona fide variables were found while testing different quality selections. These failed the quality cuts on \overline{NB} or the mean $(w1/w2)chi$ parameters due to poor data quality at one or two epochs. The 23 real high amplitude variable stars are listed in Table 1. This search is not 100% complete.

It is merely a first exploration to demonstrate the potential of the WISE multi-epoch dataset.

To search for transients, we selected sources detected at only one epoch that satisfy the following criteria for parameters in the WISE L1b source tables (all based on values for the epoch that were averaged over the individual scans): $\text{round}(NB) = 1$ (i.e. the number of deblended sources contributing to the detection averages to < 1.5) and the following conditions concerning at least one of the two passbands (W1 and W2),

$$w1mpro < 9 \text{ AND } w1snr > 5$$

$$w1chi < 5 \text{ OR } w1chi < \frac{(w1snr - 3)}{7}$$

$$w2mpro < 9 \text{ AND } w2snr > 5$$

$$w2chi < 5 \text{ OR } w2chi < (0.1 \times w2snr - 0.3)$$

This selection yielded 104 transient candidates, of which only one, VVV-WIT-01, passed visual inspection. This transient search is likely to be more complete than our variable star search, being less affected by data quality issues that affect only one or two epochs.

Table 1. Visually confirmed high amplitude WISE variable stars in IRDCs

No.	Name	RA	Dec	$\overline{W1}$	$\overline{W2}$	$\Delta W1$	$\Delta W2$	Type	Period (d)	Notes and other identifications
1	WISEA J134444.02-623127.4	206.1835	-62.5244	9.39	6.35	2.32	2.58	AGB?	650	[RMB2008] G309.0355-00.2858
2	WISEA J142238.82-611553.7	215.6620	-61.2650	8.01	5.53	2.16	1.94	YSO		Main subject of this work
3	WISE J142345.85-612540.7	215.9411	-61.4282	13.01	11.44	3.74	3.67	YSO		
4	WISEA J154914.33-543423.6	237.3096	-54.5733	11.41	9.53	2.86	2.18	YSO		
5	WISEA J163957.05-462614.2	249.9877	-46.4374	8.69	5.89	1.93	2.16	YSO		
6	WISEA J165035.47-444959.5	252.6479	-44.8332	10.02	6.83	2.47	2.19	AGB?	700	[RMB2008] G340.7273-00.2234
7	WISEA J165250.41-443908.4	253.2103	-44.6524	10.59	6.96	1.83	2.11	AGB?	800	[RMB2008] G341.1209-00.4163
8	WISEA J165344.39-432819.2	253.4351	-43.4720	12.96	10.51	5.26	3.28	YSO		VVVv746, [RMB2008] G342.1371+00.2054
9	WISEA J170547.35-411307.5	256.4473	-41.2187	12.57	9.78	3.21	2.27	YSO		
10	WISEA J171910.90-390226.9	259.7952	-39.0409	12.05	9.83	3.28	2.16	YSO		VVVv422
11	WISEA J172258.05-370309.6	260.7421	-37.0526	7.88	6.53	2.25	1.81	AGB?	550	IRAS 17195-3700
12	WISEA J181041.21-191040.2	272.6718	-19.1778	11.09	9.34	2.97	2.31	AGB?	375	[RMB2008] G011.3064-00.0637
13	WISEA J181426.60-172921.9	273.6110	-17.4894	8.58	6.16	1.73	2.31	YSO		[RMB2008] G013.2154-00.0350. YSO candidate in Marton et al.(2016).
14	WISEA J181704.22-162554.0	274.2676	-16.4318	9.72	6.59	2.01	1.96	AGB?	900	
15	WISEA J181725.67-170211.7	274.3572	-17.0366	12.24	8.61	3.25	2.09	YSO		[RMB2008] G013.9529-00.4460
16	WISEA J181736.79-165006.2	274.4031	-16.8351	8.37	6.98	2.51	1.74	AGB?	580	
17	WISEA J181832.84-133239.3	274.6368	-13.5443	11.54	9.23	2.61	2.6	YSO		[RMB2008] G017.1562+00.9715
18	WISEA J181849.10-140818.3	274.7048	-14.1384	7.87	5.54	1.63	2.06	AGB?	900	[RMB2008] G016.6638+00.6324
19	WISEA J182025.44-163608.8	275.1059	-16.6024	10.61	9.43	2.6	2.28	YSO		[RMB2008] G014.6746-00.8724
20	WISEA J182712.94-124904.8	276.8040	-12.8180	7.46	5.63	1.68	2.02	YSO		[RMB2008] G018.7877-00.5509
21	WISEA J185720.27+015711.8	284.3345	1.9533	7.76	6.87	3.72	3.48	YSO		[RMB2008] G035.3429-00.4212. 4.6 mag fainter in GLIMPSE
22	WISEA J190424.69+054106.8	286.1031	5.6853	10.03	8.58	2.03	2.01	YSO?		YSO candidate in Marton et al.(2016)
23	WISEA J195146.18+272458.7	297.9423	27.4163	9.58	7.42	2.04	1.28	YSO		[RMB2008] G063.9380+00.2509. Monotonic fader. YSO candidate in Marton et al.(2016).

2.2 Summary of variable star findings

YSOs dominate the Galactic population of high amplitude near infrared variable stars [Contreras Peña et al. \(2014, 2017\)](#); [Lucas et al. \(2017\)](#). Given that our search was focussed on IRDCs we would therefore expect most of the 23 variable stars in [Table 1](#) to be YSOs. The WISE W1 and W2 light curves show no sign of periodicity in most cases and many of them were previously identified as YSO candidates in infrared colour and SED-based searches [Robitaille et al. \(2008\)](#); [Marton et al. \(2016\)](#) or by the time domain search of ([Contreras Peña et al. 2017](#)) using the VISTA Variables in the Via Lactea survey (VVV, [Minniti et al. 2010](#)). In [Table 1](#) we give an initial classification for each source as either a YSO or a candidate pulsating Asymptotic Giant Branch (AGB) star, based mainly on the WISE light curves and the VVV/VVVx¹ light curves that are available for 20 of the 23. The AGB stars are Long Period Variables, with periods of several hundred days. These luminous sources are a significant source of contamination at bright magnitudes in variable YSO searches and it is sometimes difficult to distinguish them from YSOs with periodic variability (see [Contreras Peña et al. 2017](#)). Sources 13, 20 and 23 in [Table 1](#) were listed as possible AGB stars by [Robitaille et al. \(2008\)](#) but with the benefit of time domain data we prefer a YSO classification for these aperiodic sources, two of which were classified as YSOs by [Marton et al. \(2016\)](#).

It is evident from [Table 1](#) that the WISE mission provides a trove of valuable data for detection of highly variable YSOs in the Galactic plane. We note that the very red colours (typically $1 < W1 - W2 < 4$) of the 23 variable stars imply that warm circumstellar matter is present in all cases, consistent with either a YSO or an AGB star with a high mass loss rate. The colours cannot be explained solely by extinction in the IRDCs because the mid-infrared extinction law is quite shallow in the WISE passbands ([Koenig & Leisawitz 2014](#)) and the measured optical depth of the IRDCs has a mean of only X at $8 \mu\text{m}$. This optical depth corresponds to a colour excess of only $E(W1 - W2) = Y$, using the infrared extinction data from [McClure \(2009\)](#).

3 WISEA J142238.82-611553.7

3.1 Discovery and light curve

Source 2 in [Table 1](#) was picked out as an object of special interest after cross-matching the 23 variable stars with the *Spitzer*/GLIMPSE and GLIMPSE-II Point Source Archives ([Churchwell et al. 2009](#)). Most sources have similar brightness (within 1 mag) in the IRAC I2 ($4.5 \mu\text{m}$) passband and the W2 ($4.6 \mu\text{m}$) passband but source 2 (=WISEA J142238.82-611553.7, hereafter WISE 1422-6115) was brighter by 8.0 mag at the brightest WISE epoch (2014 February 17) than it was at the GLIMPSE epoch (2004 March 11). At $\lambda \approx 3.5 \mu\text{m}$ the rise in brightness from 2004 to 2014 was slightly smaller at 7.3 mag, based on a simple comparison of the I1 ($3.6 \mu\text{m}$) and W1 ($3.3 \mu\text{m}$) magnitudes. Ta-

Table 2. Time series photometry for WISE 1422-6115

MJD	W1	σ_{W1}	W2	σ_{W2}
55243.6	7.38	0.04	5.70	0.08
55422.2	7.30	0.04	5.52	0.13
56705.7	7.16	0.08	5.07	0.15
56886.9	7.58	0.07	5.37	0.14
57070.4	7.98	0.03	5.42	0.14
57245.7	8.23	0.03	5.75	0.11
57434.6	8.44	0.03	5.97	0.10
57604.7	8.62	0.03	6.24	0.08
57798.8	8.73	0.03	6.29	0.08
57967.3	8.97	0.03	6.55	0.07
58165.9	9.18	0.01	6.69	0.06
58328.5	9.44	0.01	6.93	0.05
58530.1	9.65	0.01	7.07	0.04
58692.7	9.94	0.01	7.31	0.04
MJD	W3	σ_{W3}	W4	σ_{W4}
55243.6	4.35	0.01	3.01	0.02
55422.2	4.24	0.03		

ble 2² lists the multi-filter WISE photometry at each epoch; for each passband we calculated the median magnitude of the individual scans at each epoch, to minimise the effect of occasional outlying data points.

Another star, source 21, brightened by 4.6 mag at $4.5 \mu\text{m}$ between 2004 and 2014. This object (SIMBAD identification [RMB2008] G035.3429-00.4212) was listed as a YSO candidate in [Robitaille et al. \(2008\)](#). We do not discuss it further here.

WISE 1422-6115 is projected only $5.7''$ from the centre of a small IRDC (SDC 313.671-0.309, equivalent radius $8.9''$) from the list of ([Peretto & Fuller 2009](#)). This IRDC has a compact far infrared and submillimetre counterpart in the form of a cold *Herschel*/HiGal molecular cloud core, HIGALBM 313.6699-0.3092, listed in the catalogue of ([Elia et al. 2017](#)) as having a fitted temperature and mass of 15.8 K and mass of $53 M_{\odot}$, respectively. Together with other local star formation indicators (see section 3.5) the presence of a large mass of cold matter centred within $4''$ of the WISE source (based on the HiGal $250 \mu\text{m}$ coordinates given by [Molinari et al. 2016](#)) verifies that this is a pre-main sequence event.

In [Figure 1](#) we plot the time series photometry and upper limits from *Spitzer*, WISE and the $2.15 \mu\text{m}$ data from VVV/VVVx, the Two Micron All Sky Survey (2MASS) and DENIS. These additional photometry are given in [Table A](#), along with mid-infrared photometry from *Akari*/IRC and in [Table A2](#) the far infrared/submillimetre photometry from *Herschel*/HiGal ([Molinari et al. 2010](#)). The 2MASS image from 2000 March 12 provides an upper limit of $K_s = 15.0$

² Note to [Table 2](#). For W1 and W2 we used the table at http://wise2.ipac.caltech.edu/docs/release/neowise/expsup/sec2_1civa.html for saturation corrections; this added ~ 0.5 mag to the brightest W2 data points. We give the error as the larger of the uncertainty on the saturated correction and the standard error on the mean derived from the individual scans at each epoch, the latter being an approximation to the standard error on the median. One highly discrepant scan was removed from the second W3 measurement.

¹ VVVx is the extension of the VVV survey, in duration and area [Minniti 2016](#)

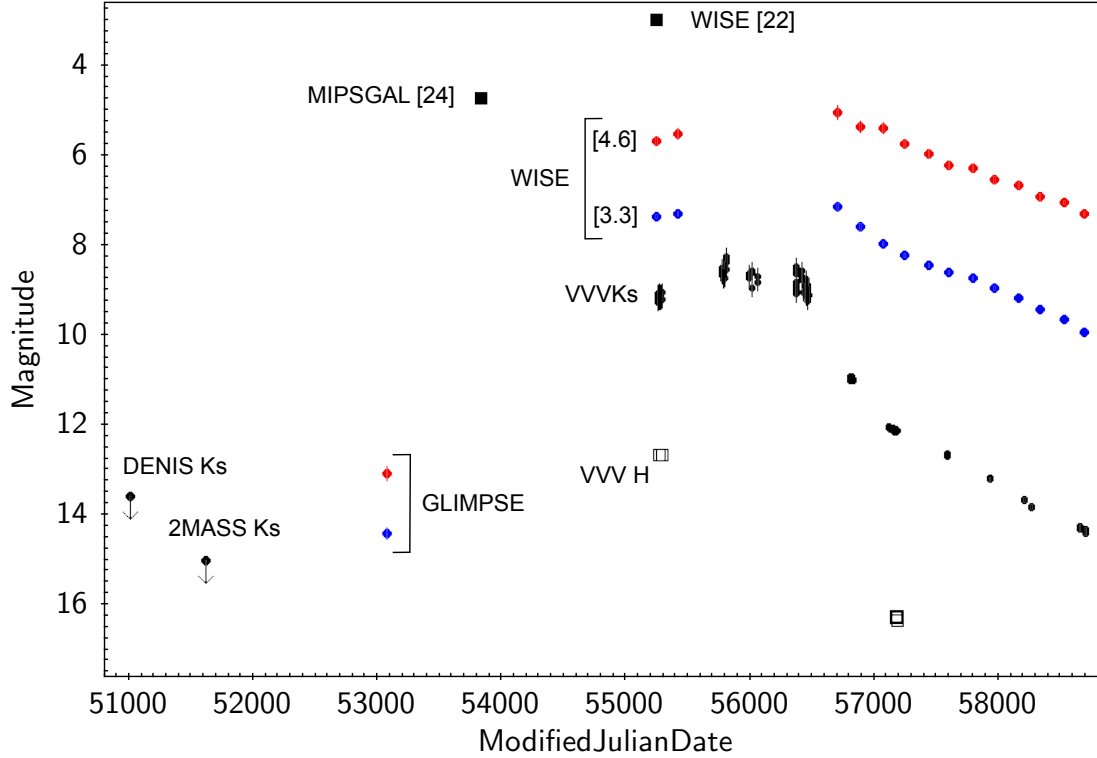


Figure 1. Multiwavelength light curves for WISE 1422-6115. The outburst appears to have begun between the GLIMPSE epoch in March 2004 and the MIPS GAL epoch in April 2006 (see main text). In 2019 the K_s magnitude remains brighter than the 2MASS upper limit from 2000, implying that the outburst duration exceeds 13 yr. The three year gap in the WISE data is due to the inactive period of the satellite between the initial WISE mission in 2010 and the subsequent NEOWISE mission.

(determined by inspecting the image and noting the faintest sources detected in the field in the 2MASS Point Source Catalogue and the 2MASS Rejects Catalogue). VVV/VVVx covers the 2010–2019 time period: we provide 157 K_s data points based on the VVV pawprint image stacks, after discarding images with seeing $>1.2''$ and a few highly discrepant data points. There were four contemporaneous image stacks at each epoch (from adjoining VVV tiles d051 and d052) each showing numerous adjacent stars for visual comparison, which made it easy to reject the outlying data. WISE 1422-6115 is spatially resolved in VVV/VVVx images, showing a cometary morphology on a scale of several arc seconds, see Figure 2. The source was also saturated near maximum brightness but fortunately the flux profile is strongly peaked so for comparison with 2MASS we were able to apply a simple saturation correction procedure to measure the brightness of the central flux peak, with ~ 0.2 mag uncertainty, see Appendix ???. The brightest VVV measurements were $K_s \approx 8.3$ on 2011 September 5. We calculated the magnitude in an $8''$ diameter aperture on this date to give a best estimate of the integrated flux: the integrated K_s magnitude is only 0.05 mag brighter than the value quoted above. However, the cometary nebula makes a larger contribution to the integrated J and H magnitudes (measured in 2010) which is relevant for SED modelling (see section 3.5).

Inspection of Figure 1 indicates that the outburst began between the GLIMPSE epoch in March 2004 and the *Spitzer*/MIPSGAL epoch in April 2006 (Rieke et al. 2004;

Carey et al. 2009). The $[8.0]-[24]$ colour is $[8.0]-[24]=6.83$: the Robitaille et al. (2008) catalogue of intrinsically red *Spitzer* sources shows that this would be an extreme outlier for a non-variable YSO. In 2019 the K_s magnitude remains brighter than the 2MASS upper limit from 2000, implying that the outburst duration exceeds 13 yr. The amplitude of the post-outburst decline is generally greater at shorter wavelengths. The general trend towards higher amplitude at shorter wavelengths also indicates that the amplitude in K_s may therefore have been greater than the 8 mag change measured at $\lambda \approx 4.5 \mu\text{m}$. The 2MASS upper limit tells us only that $\Delta K_s > 6.7$ mag.

The peak of the outburst was fairly flat from 2010–2013. However, fairly rapid ~ 0.4 mag variations in the K_s magnitude of the central peak did occur: over a one day interval in 2013 (MJD=56374 to 56375) and over the 23 day interval in 2011 leading up to the maximum observed brightness at MJD=55809.0. Infrared variations at this level are common in embedded YSOs due to changes in extinction or accretion rate (if accretion is magnetically controlled). However, the 23 day timescale is rather longer than conventional variations in magnetically controlled accretion rate (Romanova et al. 2008).

3.2 Spatially resolved structure

Figure 2 shows that most of the extended nebulosity faded at approximately the same rate as the central flux peak, as

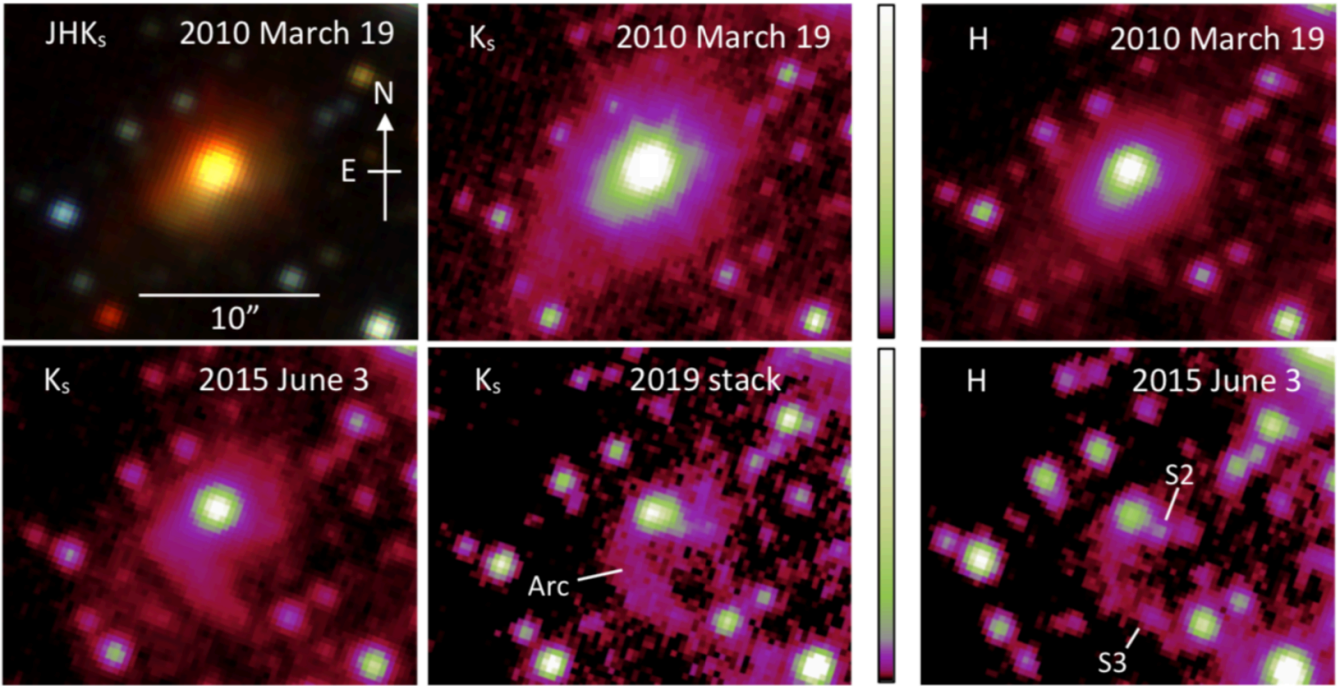


Figure 2. VVV near infrared Images WISE 1422-6115. All panels have the same spatial scale and equatorial orientation. The upper left panel is a three-colour image (red is K_s , green is H and blue is J). This image taken just below maximum brightness shows the bright central flux peak and the faint cometary nebula extending to the southeast. The other five panels are false-colour images in the K_s and H passbands, scaled to show the changing morphology as the outburst faded (see main text). The K_s and H images use a colour map that emphasises faint features (see the vertical colour bars between the the centre and right panels). The images have a linear scaling from the sky background level to approximately the peak brightness of the brightest star in each panel.

expected for a reflection nebula. Near maximum brightness (in 2010–2013) the cometary nebula extended $\sim 10''$ to the southeast in K_s and H . As the outburst faded in later years, the morphology changed. A faint arc of nebulosity curving to the south of the central source is seen in the 2015 H image and the 2019 K_s image stack³, extending as far as the faint star labelled “S3” in the 2015 H image. This arc gradually becomes more visible in the K_s images from 2015 onwards, as the rest of the nebula fades. Other faint stars projected within the nebula become visible as the outburst fades, e.g. the star labelled “S2” adjacent to the central flux peak. (This is a fairly crowded Galactic star field and most stars in the images are probably in the foreground since they have relatively blue colours (see section ??). The arc of nebulosity appears to have faded only slightly between 2015 and 2019 and it may have been present in 2010, simply hidden by the bright reflection nebula. This arc might possibly arise in shocked gas, in a situation where shocks created by interaction of a high velocity and low velocity gas in an outflow produce UV line emission that is then reprocessed to lower frequencies. Its greater prominence in H than in K_s in the

2015 image suggests that it suffers less reddening than the rest of the nebula.

The size of the structure is surprising. The 2010 and 2015 K_s images and the 2010 H image show a cometary nebula of the kind commonly seen in class I YSOs when light is scattered from the walls of a cavity in the circumstellar envelope, attributable to a molecular outflow (Whitney & Hartmann 1993). However, the distance of the system is $d \approx 2.6$ kpc (see sections 3.5 and ??) so the $\sim 10''$ extent of the nebula to the southeast of the central source corresponds to 26 000 au (0.13 pc). This is unrealistically large for a circumstellar envelope but not unusual for either a molecular cloud core or a molecular outflow. The fainter extremities of the nebula might arise from scattering by dust in an outflow (Lucas & Roche 1997; Chrysostomou et al. 2007). Alternatively, the outer portions of the HiGal submm cloud core may be dense enough to be observable in scattered light. The 2010 images and the 2015 K_s image have a sudden drop in surface brightness 4 to 4.5'' southeast of the central peak. Elia et al. (2017) measured a beam-deconvolved radius of 4.5'' at 250 μm for the cloud core so the drop in K_s surface brightness at a similar radius might correspond a drop in the density of the cloud core. The alternative that the drop in flux occurs at the edge of a rather large YSO envelope (10 000–12 000 au radius). The HiGal radius measurement would appear to be uncertain due to the known issue of variation in beam-deconvolved source sizes as a function of wavelength (Elia et al. 2017) and the fact that the size is much less than the *Herschel* beam size in this case. Nonetheless,

³ Most of the single-band images in Figure 2 are cut-outs from VVV tile stack images, with 80 s time on source, taken during multi-colour observing blocks in 2010 and 2015 (Saito et al. 2012). Other VVV/VVVx observing blocks have shallower K_s images so the “2019” image was constructed from a stack of the 12 (8 s) K_s pawprint stack images taken at the three epochs of observation in 2019, giving a combined exposure time of 96 s.

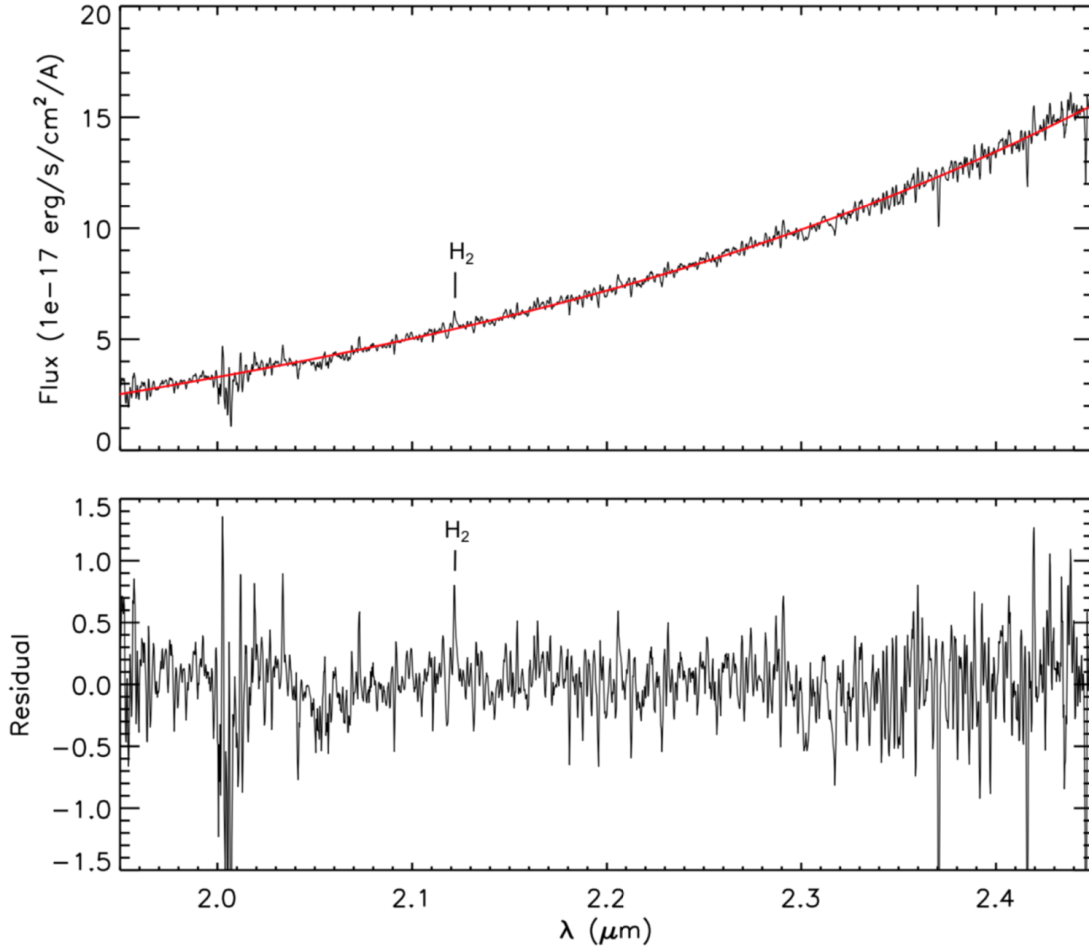


Figure 3. SOAR/ARCoIRIS spectrum of WISE 1422-6115. (*Upper panel*): spectrum with the continuum fit by a cubic polynomial. (*Lower panel*): residual after subtracting the continuum fit. The (1-0) S(1) emission line of H_2 is weakly detected at 2.12 μm .

the spatial scale resembles that of a cloud core better than a YSO envelope (see Pokhrel et al. 2018, for an illustration of the hierarchy of size scales in star formation).

3.3 Spectrum

An infrared spectrum of WISE 1422-6115 was obtained by co-author JE on the night of 2019 July 18/19 with the ARCoIRIS spectrograph on the 4-m Southern Astrophysical Research Telescope (SOAR) at Cerro Pachon, Chile. ARCoIRIS is a cross-dispersed spectrograph providing a spectral resolution $R=3500$ across the 0.8–2.5 μm wavelength range, with a fixed slit width of 1.1". The integration time was 48 minutes on source, broken down into 16 three minute exposures. The spectra were reduced with the Spextool 4.1.0 pipeline, with independent reductions by coauthors SP and PWL providing essentially identical results. The A0V star HIP 76244 was used for telluric correction. The Spextool pipeline fits and removes the sky background in the dispersed images without the need for nodding the telescope between two positions and subtracting spectra. However, two separate nod positions were used in an ABBA pattern, enabling quick subtraction during the observations to con-

firm target acquisition and helping to guard against array defects.

The spectrum is shown in Figure 3, where we see a continuum that rises rapidly with increasing wavelength. There is a weak detection of the (1-0) S(1) emission line of H_2 at wavelength $\lambda = 2.1215 \mu\text{m}$, slightly blue-shifted from the rest wavelength of $\lambda = 2.1218 \mu\text{m}$. While the line is weak (the equivalent width is $-1.0 \pm 0.4 \text{ \AA}$) it is detected in four separate subsets of half the data (i.e. position A observations, position B observations, the first eight exposures and the last eight exposures) so it appears to be a genuine feature. There is no sign of the usual spectroscopic features associated with FU Ori-type or EX Lupi-type outbursts (CO and H_2O in absorption in the former type, CO emission and Bry emission in the latter). This is not surprising because by 2019 the outburst had faded by 6 mag from its peak brightness in K_s . However, the detection of weak 2.12 μm H_2 emission serves to support the interpretation of the system as a YSO because this line is typical of class I YSOs (e.g. Greene & Lada 1996; Doppmann et al. 2005) but rarely seen in other types of star. Other than YSOs, this emission line is seen in protoplanetary nebulae but these objects are not associated with high amplitude variability. Amongst YSOs, it is much

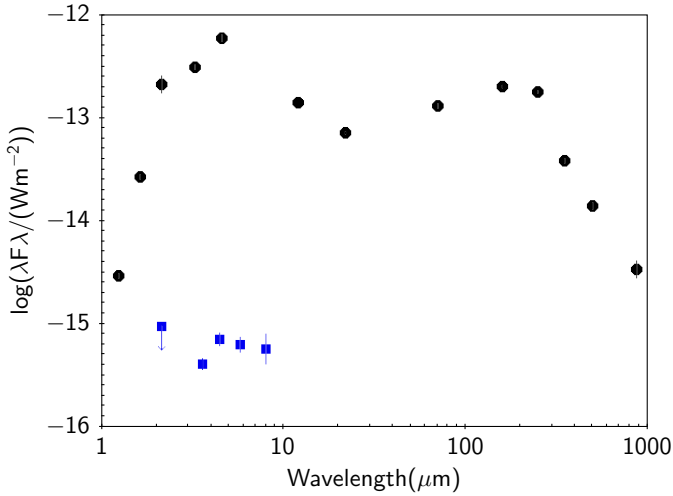


Figure 4. SED of WISE 1422-6115 and the surrounding cold cloud core. The VVV, WISE and HiGal data are roughly contemporaneous, all taken in 2010, when the outburst was slightly below the peak as measured in K_s . We also include $870\ \mu\text{m}$ ATLASGAL photometry from 2008. The form of this double peaked SED does not resemble the SED of a normal embedded YSO: the near to mid-infrared peak is most likely due to a dramatic episodic accretion event in the inner disc whilst the far infrared/submm peak is best fitted by emission from a massive cold cloud core on a larger spatial scale. The latter peak is probably enhanced a little by the warming effect of the outburst on the whole cloud core.

more commonly seen in class I YSOs than class II systems (Greene & Lada 1996).

The radial velocity of the H_2 emission is measured as $v_{\text{LSR}} = -66 \pm 10\ \text{km s}^{-1}$, after applying the heliocentric correction and correcting for the sun’s motion relative to the Local Standard of Rest (Schönrich et al. 2010). H_2 emission from YSOs can have a velocity that is significantly offset from the system’s reference frame (e.g. Guo et al. 2020) so it is unsafe to use this to calculate a kinematic distance. If we nonetheless employ a constant Galactic rotation model with $\Theta_0 = 236\ \text{km s}^{-1}$ (consistent with Reid et al. 2019), we find a kinematic distance $d \approx 5.6\ \text{kpc}$, placing the source at the tangent point with the largest possible negative velocity for this Galactic longitude ($l = 313.67^\circ$). However, our preferred distance is $d \approx 2.6\ \text{kpc}$ (see section 3.5) so it seems likely that the system is actually at a closer distance and the measured radial velocity of the H_2 line is blue-shifted relative to the system’s rest frame, as is observed in other eruptive YSOs (Guo et al., in prep). This would imply that the observed H_2 emission arises in the approaching half of a bipolar outflow rather than a disc wind.

3.4 SED

In Figure 4, we show the SED of WISE 1422-6115 and the surrounding cold cloud core from $1\ \mu\text{m}$ to $1\ \text{mm}$. Blue points are the data from GLIMPSE and the 2MASS upper limit, all taken pre-outburst. Black points are based on data taken during the bright part of outburst: VVV, WISE and *Herschel*/HiGal data were all taken in 2010, when VVV K_s and WISE W2 fluxes were only a factor of ~ 2 lower than the

highest values measured. The VVV and WISE data points were taken only a month apart (February to March 2010) but the HiGal data from Elia et al. (2017, for the core designated HIGALBM 313.6699-0.3092) are an average of several observations at more separated dates in the year. The ATLASGAL $870\ \mu\text{m}$ datum was taken in 2008, also during the bright stage of the outburst (see Figure 1). The HiGal and ATLASGAL data at $\lambda > 250\ \mu\text{m}$ were scaled to the measured size of the $250\ \mu\text{m}$ detection, a procedure adopted by Elia et al. (2017) for SED fitting for all the molecular clumps and cores in their HiGal catalogue (see that work and references therein). The VVV J , H and K_s photometry shown here are integrated fluxes measured in an $8''$ diameter aperture, for better comparison with the lower resolution WISE photometry.⁴

The pre-outburst GLIMPSE colours suggest that WISE 1422-6115 is a class I YSO: $I1-I2=1.33$, $I3-I4=0.87$ and $I2-I4=1.51$ are typical of class I YSOs in Gutermuth et al. (2009). The $I2-I3=0.64 \pm 0.23$ measurement is blue for a class I YSO, but the uncertainty allows it to be consistent with the colour space adopted by those authors. These colours provide further evidence for class I status, adding to the $2.12\ \mu\text{m}$ H_2 emission line mentioned earlier. In outburst, the $1-22\ \mu\text{m}$ SED can be fitted by a range of stage 2 (envelope-free) YSO models with the (Robitaille et al. 2007) model grid but the far infrared signature of any envelope that may be present is obscured by the cloud core so these fits are of little value. (As noted earlier, the near infrared cometary nebula resembles a class I YSO but the large spatial scale suggests reflection from a dense cloud core rather than a protostellar envelope).

The HiGal cloud core appears very compact in all the HiGal 70 to $500\ \mu\text{m}$ images. Elia et al. (2017) fit a beam-deconvolved diameter of $9.09''$ at $250\ \mu\text{m}$. Their grey-body SED fit to the 170 to $870\ \mu\text{m}$ HiGal and ATLASGAL data gives a mass $M = 53\ M_\odot$, temperature $T = 15.8 \pm 0.2\ \text{K}$ and optical depth unity at wavelength $\lambda_0 = 81.5\ \mu\text{m}$. (Their adopted distance, $3.13\ \text{kpc}$, is comparable to our preferred distance of $2.6\ \text{kpc}$). This high mass and cold temperature make it clear that at wavelength $\lambda > 100\ \mu\text{m}$ the SED is dominated by a cloud core rather than a circumstellar envelope. The double-peaked SED, with the higher peak in the near to mid-infrared, does not resemble a normal class I or class 0 YSO: we confirmed this by trying unsuccessfully to fit it with the (Robitaille et al. 2007) SED fitting tool (Python SEDFITTER version).

We regard the beam-deconvolved diameter of the core as uncertain since it is much smaller than the *Herschel*/HiGal beam at $250\ \mu\text{m}$ (see 3.2). (The published value is consistent with the size of the darkest portion of the IRDC as it appears in the GLIMPSE $I4$ image but smaller by a factor of two than the IRDC equivalent radius given by Peretto et al. (2016)). Therefore we performed our own grey-body fits of the 170 to $870\ \mu\text{m}$ SED to check the published parameters, in a similar manner to Ward-Thompson & Robson (1990).

⁴ The integrated VVV magnitudes ($J=15.31$, $H=12.18$, $K_s=9.11$, based on data from 2010 March 19) are significantly brighter in J and H than the point source magnitudes given in Table A ($J=16.06$, $H=12.65$, $K_s=9.17$) since the cometary nebula makes a substantial contribution up to a $4''$ radius, though not beyond that.

We initially added the core’s solid angle on the sky, Ω , and then also the opacity power law index β as free parameters ($\beta = 2$ was adopted by [Elia et al. 2017](#)). We found that β , Ω and λ_0 were not well constrained by the data but the temperature is well constrained, with minimum chi-squared values corresponding to $T = 15$ K for a 4 parameter fit, or $T = 16$ K if we set $\beta = 1.8$, in close agreement with [Elia et al. \(2017\)](#). Temperature is the key parameter that determines the derived mass so our mass estimates were of the same order as that of [Elia et al. \(2017\)](#).

The higher luminosity of the shorter wavelength peak is consistent with the YSO outburst model of [Johnstone et al. \(2013\)](#), wherein an outburst in the inner disc greatly raises the near and mid-infrared flux but has a gradually decreasing effect at longer wavelengths. In their model, radiation is reprocessed in the circumstellar envelope (assuming there is one) with a warming effect. However, the Rayleigh-Jeans tail of a Planckian SED flux scales only linearly with temperature, leading to a smaller effect at submm wavelengths. In WISE 1422-6115, the pre-outburst infrared luminosity (blue points in Figure 4) is negligible compared to the luminosity of the massive cold cloud core. In 2010, the in-outburst infrared luminosity measured at $1.25 \mu\text{m}$ to $22 \mu\text{m}$ was $L = 178(d/2.6\text{kpc})^2 L_\odot$. This exceeds the cold core’s luminosity from $70\text{--}870 \mu\text{m}$ ($L = 59(d/2.6\text{kpc})^2 L_\odot$) by a factor of three, perhaps rising to a factor of six at the K_s peak in 2011, or even more if we allow for infrared extinction. The core is therefore likely to have been heated by a few degrees. The heating efficiency would depend somewhat on whether the radiation is first reprocessed by a smaller circumstellar envelope and re-emitted at submm wavelengths where the optical depth of the core is low.

The 2010 luminosity measured from the $1.25 \mu\text{m}$ to $870 \mu\text{m}$ SED is $L = 263(d/2.6\text{kpc})^2 L_\odot$, using trapezium rule summation. Considering the very small ratio of pre-outburst to in-outburst luminosity in the $3\text{--}5 \mu\text{m}$ region, this tell us that the progenitor is a low mass YSO. Even allowing for extinction by the IRDC, the quiescent luminosity is likely to be of order $1 L_\odot$ or less, even if most of the flux were emitted in the far infrared.

The decline in the (in-outburst) flux from $4.6 \mu\text{m}$ to $22 \mu\text{m}$ indicates that the outburst takes place in the inner disc and radiation is not very efficiently transferred to larger disc radii. Alternatively, there might be a gap in the disc. Using $\lambda T = 3.67 \text{ mm K}$ at the peak of a Planckian SED, the infrared peak at $4.6 \mu\text{m}$ implies $T \sim 800$ K. Inserting this value in the equation $L = 2\pi R^2 \sigma T^4$ gives a radius $R = 4.6 \text{ au}$ for the outburst. In fact the radius may be even larger since there is almost certainly substantial infrared extinction towards the source: the ratio of fluxes in W2 to W1 is not consistent with a Planckian spectrum at the temperature of 800 K. Either substantial extinction or a substantially lower temperature is required. A broad spread of temperatures is typical in an accretion disc but given the constraint of the SED peak wavelength, it is hard to avoid the conclusion that there are a few magnitudes of extinction in the W2 passband. This is reasonable to expect for the inner disc of a class I YSO located inside a dense cloud core.

The mid-infrared decline in the SED is unusual for HiGal protostellar cores with AllWISE counterparts in the [Elia et al. \(2017\)](#) catalogue: using their definition of cores as bodies with radii $r < 0.1 \text{ pc}$, we found that during outburst

WISE 1422-6115 was a blue outlier with $W2 - W4 = 2.68$, compared to $4 < W2 - W4 < 9$ for most other cores. Unsurprisingly, it is one of the brightest sources in W2 ($4.6 \mu\text{m}$).⁵

3.5 Wider environment and distance

In Figure 5 we illustrate the star forming environment around WISE 1422-6115. In the upper panel (a GLIMPSE $8 \mu\text{m}$ image taken pre-outburst), WISE 1422-6115 is seen as a very faint source at the edge of the IRDC G313.671-0.309, which in turn appears as an unremarkable small patch at the edge of a much larger dark cloud. We identify this large cloud as PGCC G313.73-00.31 from the list of “Planck Galactic Cold Clumps” ([Planck Collaboration et al. 2016](#)). Those authors carefully calculate distances to the molecular clouds in their list using several methods, finding $d = 2.72 \pm 0.82 \text{ kpc}$ for PGCC G313.73-00.31. This was an extinction-based distance based on a comparison of the colours and magnitudes of all stars in the region with the prediction of the Besancon Galactic population models ([Robin et al. 2003](#)). They noted that the result was consistent with a near kinematic distance of 3.15 kpc for the IRDCs in the vicinity ([Simon et al. 2006](#); [Jackson et al. 2008](#)). Other authors have measured similar radial velocities for cold cloud cores within the Planck clump ([Vasyunina et al. 2011](#); [Purcell et al. 2012](#)), the former work specifies a distance $d \approx 3.3 \text{ kpc}$. The middle and lower panels of Figure 5 give a wider field view (16 arcminute width). The dark cloud is seen to extend further to the northeast in WISE three colour image (the whole dark area corresponding to dark cloud no. 6082 of [Dobashi \(2011\)](#)). WISE 1422-6115 appears bright in the WISE image and the HiGal cold cloud core (HIGALBM 313.6699-0.3092) is seen at the same location in the lower panel.

Other bright regions in the middle and lower panels of Figure 5 correspond to star formation activity at a kinematic distance similar to those mentioned above. E.g. IRAS 14188-6054 is an HII region containing a 6.7 GHz methanol maser (MMB G313.705-00.190 ([Green et al. 2012](#)) and the associated ATLASGAL cloud core AGAL 313.706-00.191. The ATLASGAL team preferred a near kinematic distance of $3.0_{-0.5}^{+0.6} \text{ kpc}$ ([Wielen et al. 2015](#)) whereas the MALT90 survey team preferred the far kinematic distance of 8.5 kpc ([Whitaker et al. 2017](#)).

Figure 6 illustrates our own extinction-based distance calculation, a red clump giant distance ([López-Corredoira et al. 2002](#)) based on the giant branch as measured in the K_s vs $J - K_s$ colour magnitude diagram (CMD) constructed from the 2MASS Point Source Catalogue. (VVV data could not be used for this because the cloud is too nearby, causing foreground stars at the extinction discontinuity to saturate). We plotted a map of three-filter detections (J, H, K_s), shown in the left panel of Figure 6, and found that the dark cloud area seen in the middle panel of Figure 5 corresponds to a region where very few red stars are present. This region appears blue in the map of detections,

⁵ Our cross-match to AllWISE found eight HiGal “protostellar cores” with much brighter and somewhat bluer WISE counterparts than WISE 1422-6115 ($W2 < 0$, $W2 - W4 < 2.5$) but seven of these are listed in the SIMBAD database as evolved stars, e.g. OH/IR stars and only one, CRL 2136, is a protostellar object.

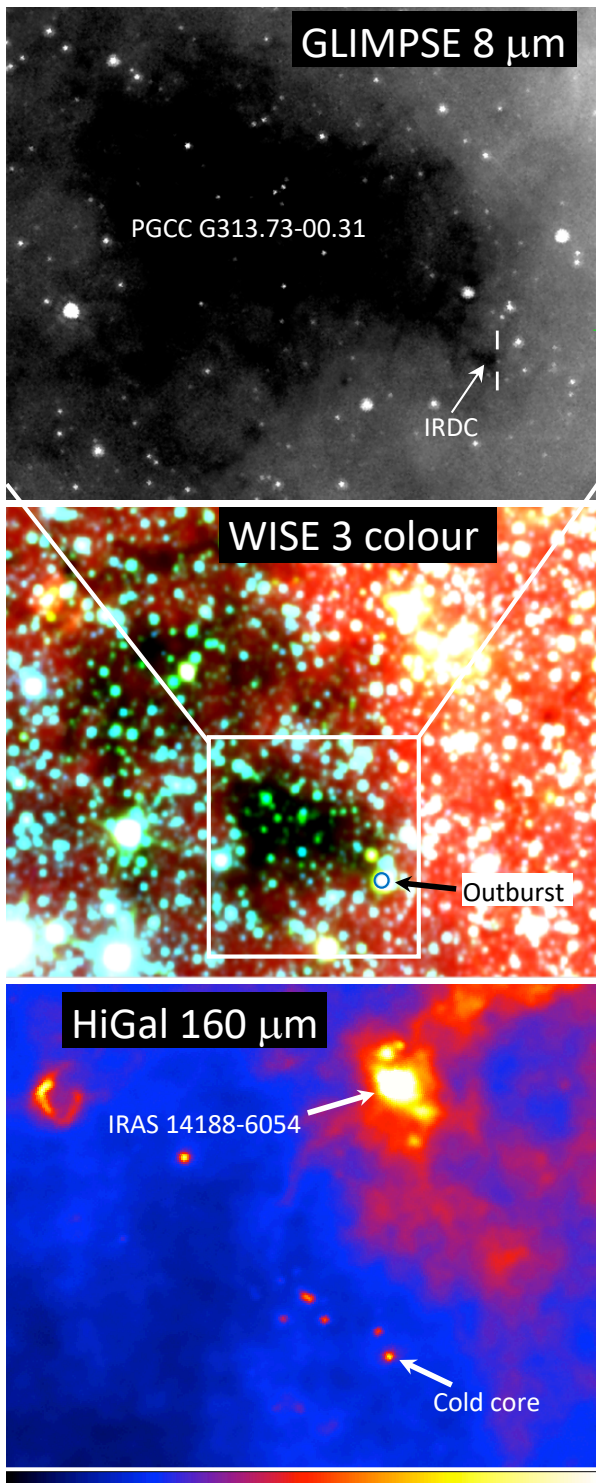


Figure 5. The wider environment. All images have equatorial orientation. (*top:*) GLIMPSE 8 μm 6 \times 5 arcminute image taken pre-outburst, in 2004. WISE 1422-6115 is faintly seen, between the vertical white markers. The IRDC (G313.671-0.309) is the adjacent small dark patch and the Planck cloud PGCC G313.73-00.31 dominates the image as a dark region. (*middle:*) WISE 16 \times 12 arcminute three colour image (blue: 3.4 μm , green: 4.6 μm , red: 12 μm) taken in 2010. The erupting YSO (marked with an arrow and a blue circle) was prominent. (*bottom:*) HiGal 160 μm 16 \times 12 arcminute false colour image, with a linear stretch (see colour bar below). The IRAS 14188-6054 HII region and the cold cloud core surrounding WISE 1422-6115 are marked.

due to the predominance of foreground stars with relatively blue colours. We traced this “blue region” by hand due to its irregular shape (in fact it is split into two adjacent areas separated by a narrow, slightly less opaque region populated by red stars). Stars in the selected blue region are plotted with open circles in the detection map. In the right panel of Figure 6 stars in the selected region are plotted as red circles. We see that the giant branch is very sparsely populated, due to a sudden cut-off near $K_s = 10.5$ mag. By contrast in the larger control region enclosing the selected area (16 arcminute radius centred on (ra, dec)=(215.8471, -61.1694), data plotted as small grey circles) the giant branch is well defined and continuous. We use this larger area as a control field to estimate the average population of red clump giants per unit magnitude in the giant branch because smaller areas have differing levels of extinction, leading to scatter in the results.

After scaling the area of the control field to the selected high extinction area of the dark cloud, we adopt the red clump giant colour, absolute magnitude and extinction law employed by Minniti et al. (2011) and we find that the cut-off occurs between 2.3 and 3.0 kpc (i.e. apparent magnitudes $K_s = 10.50$ and $K_s = 11.07$) with high confidence. At $d = 3.0$ kpc, the control field tells us that number of “missing” giant branch stars in the selected region is 5.8 ± 2.4 and the Poisson probability of a gap at $10.50 < K_s < 11.07$ is ($P(0) = 0.3\%$). We adopt a likely distance range of 2.3 to 3.0 kpc to the dark cloud, with a preferred value of 2.6 kpc. This is consistent with kinematic distances slightly in excess of 3 kpc because peculiar velocities of only a few km/s relative to the Galactic rotation curve would modify the kinematic distance by several hundred pc. Inspection of the Gaia-based distances of Bailer-Jones et al. (2018) confirms that the distance to the dark cloud is at least 2.3 kpc. The most distant stars having parallax measurements above 5σ significance have a lower distance bound of c.2.5 to 2.6 kpc in that work, at 90% confidence. If we allow for the known negative offset of order 30 mas in the current Gaia parallaxes (Lindgren et al. 2018), this translates to a minimum distance of about 2.3 kpc.

4 DISCUSSION

The 8 mag mid-infrared amplitude of the outburst is higher than that of any previously recorded episodic accretion event, in any waveband. This extreme value, together with the long duration and the mid-infrared location of the peak in the SED provide useful constraints regarding which disc instability mechanism is operating here. For example, models employing the thermal instability mechanism (Lin & Papaloizou 1985; Hartmann & Kenyon 1985; Bell & Lin 1994; Bell et al. 1995) produce a high temperature outburst in the innermost part of the disc, leading to a lower amplitude in the infrared at optical wavelengths. For comparison, the repetitive outbursts seen in dwarf novae can have optical amplitudes of several magnitudes but infrared amplitudes are generally lower. A simple cross-match of the OGLE III sample of dwarf novae Mróz et al. (2015) against the VVV 4th Data Release recovered 141 objects, amongst which the K_s variability never exceeded 3 mag.

Similarly, the magnetic gating model D’Angelo & Spruit

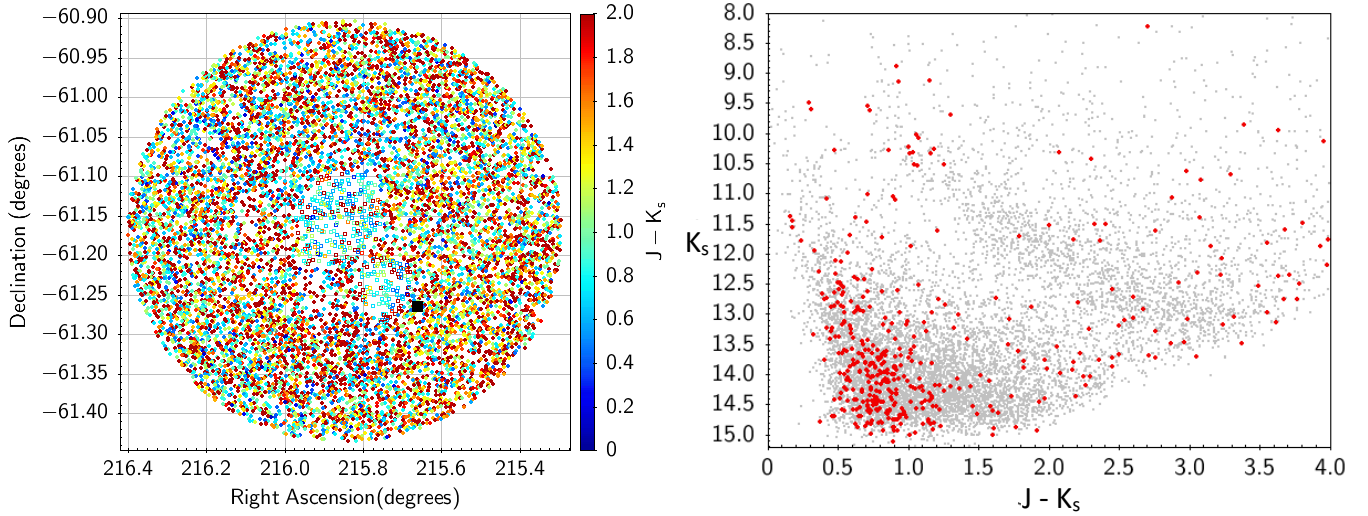


Figure 6. Red clump giant extinction-based distance to the Planck cloud PGCC G313.73-00.31. *left:* 2MASS map of sources in a 16 arcminute radius area centred on the region of highest extinction. The colour coding according to $J - K_s$ colour shows that very few red stars are visible near the centre, where the cloud is opaque. Stars are plotted with circles in the selected opaque (blue-ish) region, where foreground stars predominate. The location of WISE 1422-6115 is marked with a black square. *right:* 2MASS K_s vs. $J - K_s$ CMD for the area of the left panel. Stars in the selected opaque region are plotted in red and the rest in grey. The giant branch is well defined by the grey points but the distribution of red points in the giant branch cuts off abruptly near $K_s=10.5$. We infer a red clump giant distance to $d \approx 2.6$ kpc to the dark cloud and apply this distance to WISE 1422-6115 also.

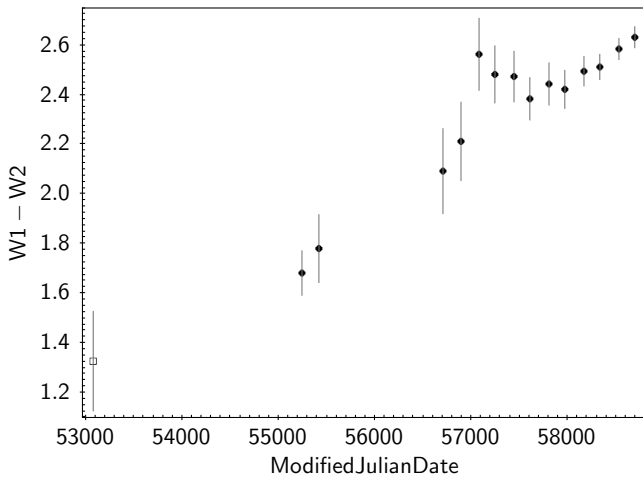


Figure 7. Evolution of the $W1 - W2$ colour of WISE 1422-6115. The earliest datum, plotted as an open square, is the GLIMPSE $I1-I2$ colour, measured pre-outburst. During outburst the overall trend was an increasingly red colour as the outburst first brightened slightly and then faded.

(2010, 2012) involves an instability near the co-rotation radius of the disc. For a typical YSO rotation period of 3 days this is 0.04 au for a $1 M_\odot$ star, far smaller than the radius of a few au derived in section 3.4. However, the scenario of fragmentation in the outer disc, followed by infall of fragments to the inner disc (Vorobyov & Basu 2006, 2010, 2015) is flexible enough to explain a release of energy at a radius of a few au.

The accretion rate during outburst can be estimated from the luminosity using the equation $L = GMM/2R_{star}$ (Shakura & Sunyaev 1973). The measured luminosity in

2010 from $1.25 \mu\text{m}$ to $22 \mu\text{m}$ was $L = 178(d/2.6\text{kpc})^2 L_\odot$. This figure does not allow for the substantial infrared extinction that we think is present towards the source (nor fact that the K_s and $W2$ fluxes were a factor of two brighter at certain times later in the outburst). If we adopt a stellar radius of $3 R_\odot$ and $M = 1 M_\odot$ then we find $\dot{M} = 7.6 \times 10^{-4} M_\odot \text{ yr}^{-1}$. Making some allowance for extinction implies a $\dot{M} =$ a few $\times 10^{-4} M_\odot \text{ yr}^{-1}$, typical of a classical FU Orionis event.

As noted earlier, the outburst declined more slowly with increasing wavelength, in the $1.6\text{--}4.6 \mu\text{m}$ range. In Figure 7 we plot the change in $W1-W2$ colour vs time. The GLIMPSE $I1-I2$ pre-outburst colour (also plotted for comparison) is similar to the WISE colour measured in 2010 if we allow for the difference between the *Spitzer/IRAC* and WISE bandpasses (Antoniucci et al. 2014). However, the outburst became redder between 2010 and the time of the brightest WISE measurements in 2014, then reddened further as the outburst began to fade, showing a blip in 2015 but a clear trend to the red from late 2016 to late 2019. The behaviour as the outburst faded can be understood simply as due to cooling of the disc but the “redder when brighter” change between 2010 and 2014 is surprising. It might be due to the outburst spreading outward through the disc, cooling slightly but increasing in luminosity as the surface area of the hottest part of the disc increased. (We noted previously that the negative gradient of the SED from $4.6\text{--}22 \mu\text{m}$ in 2010 was a sign that energy had not yet been efficiently redistributed outward in the disc by that date). Alternatively there may have been an increase in extinction that was more than counterbalanced by an increase in accretion rate.

Finally, the large size of the cometary reflection nebula requires some explanation. We have interpreted it as reflection from the massive cloud core (section 3.2) which implies that cometary nebula must be due to the structure of the

core. This may indicate that an outflow has cleared a low density cavity that extends through the core and out into the more diffuse interstellar medium. Alternatively it may simply indicate a pre-existing density gradient in the cloud core that causes regions of lower optical depth to appear better illuminated. Narrow band imaging in the 2.12 μm H_2 line or radio mapping in CO could distinguish between these two options.

5 CONCLUSIONS

We have detected 23 new highly variable mid-infrared sources ($\Delta\text{mag}>2$) in a catalogue of WISE/NEOWISE sources projected in the vicinity of IRDCs. Most of these are YSOs but about a third of these relatively bright red stars are periodic sources, more likely to be dusty Mira-like variables. Since we have searched only a very small portion of the Galactic plane, this demonstrates the potential of the ongoing NEOWISE mission for eruptive YSO science, complementing VVV/VVVx.

The most notable discovery is the 8 mag outburst in WISEA J1422-6115, a low mass YSO at a distance $d = 2.3 - 3.0$ kpc that is presumed to have undergone an episodic accretion event. In evolutionary terms, we classify it as a probable stage 1 protostar. The in-outburst luminosity of a few $\times 10^2 L_\odot$ is higher than that of the surrounding massive cold cloud core so it is possible that the core was measurably warmed by the event, though probably not enough for major changes to the cloud's chemical make-up. By contrast, the accretion disc and any surrounding circumstellar envelope would have been heated far more strongly.

The infrared luminosity is consistent with an accretion rate $\dot{M} \sim 10^{-4} M_\odot \text{yr}^{-1}$, comparable to a classical FU Orionis event. However, the 4.6 μm peak in the SED corresponds to a temperature $T \approx 800$ K. The temperature and luminosity then imply a disc radial location $r \approx 4.6$ au for the site of the burst, larger if we adjust the luminosity by allowing for extinction.

GLIMPSE, MIPS GAL, WISE and VVV data indicate that the outburst began between 2004 and 2006 and had a total duration > 13 yr. The very high amplitude, long duration and mid-infrared location of the peak in the SED help to distinguish which of the proposed physical mechanisms for YSO outbursts may have triggered instability in the accretion disc. These features of the event strongly disfavour the thermal instability mechanism and the magnetic gating mechanism (designed more to explain EXor-like events, see D'Angelo & Spruit 2010, 2012). However, the data appear to be consistent with the concept of disc fragmentation, wherein small fragments fall into the inner disc (Vorobyov & Basu 2006, 2010, 2015). The low pre-outburst luminosity of the protostar and the location inside a cold dense cloud core should lead to a low temperature in the outer disc; this would tend to facilitate fragmentation, as noted by Vorobyov & Basu (2010).

Further observations of this system are certainly desirable to more firmly establish its nature. Very high resolution submm continuum imaging with ALMA might be able to detect signs of fragmentation in the outer disc. Slightly lower resolution radio data would be able to detect the expected circumstellar envelope within the cloud core, con-

firring stage I evolutionary status. Either ^{13}CO mapping or 2.12 μm imaging in the H_2 could be used to search for an outflow and better understand the nature of the large cometary reflection nebula.

ACKNOWLEDGEMENTS

REFERENCES

- Antonucci S., Giannini T., Li Causi G., Lorenzetti D., 2014, *ApJ*, **782**, 51
- Audard M., et al., 2014, *Protostars and Planets VI*, pp 387–410
- Bailer-Jones C. A. L., Rybizki J., Fousneau M., Mantelet G., Andrae R., 2018, *AJ*, **156**, 58
- Bell K. R., Lin D. N. C., 1994, *ApJ*, **427**, 987
- Bell K. R., Lin D. N. C., Hartmann L. W., Kenyon S. J., 1995, *ApJ*, **444**, 376
- Benjamin R. A., et al., 2003, *PASP*, **115**, 953
- Caratti o Garatti A., et al., 2016, *Nature Physics*, **13**, 276
- Carey S. J., et al., 2009, *PASP*, **121**, 76
- Chrysostomou A., Lucas P. W., Hough J. H., 2007, *Nature*, **450**, 71
- Churchwell E., et al., 2009, *PASP*, **121**, 213
- Contreras Peña C., et al., 2014, *MNRAS*, **439**, 1829
- Contreras Peña C., et al., 2017, *MNRAS*, **465**, 3011
- D'Angelo C. R., Spruit H. C., 2010, *MNRAS*, **406**, 1208
- D'Angelo C. R., Spruit H. C., 2012, *MNRAS*, **420**, 416
- Dobashi K., 2011, *PASJ*, **63**, S1
- Doppmann G. W., Greene T. P., Covey K. R., Lada C. J., 2005, *AJ*, **130**, 1145
- Elia D., et al., 2017, *MNRAS*, **471**, 100
- Green J. A., et al., 2012, *MNRAS*, **420**, 3108
- Greene T. P., Lada C. J., 1996, *AJ*, **112**, 2184
- Guo Z., et al., 2020, *MNRAS*, **492**, 294
- Gutermuth R. A., Megeath S. T., Myers P. C., Allen L. E., Pipher J. L., Fazio G. G., 2009, *ApJS*, **184**, 18
- Hartmann L., Kenyon S. J., 1985, *ApJ*, **299**, 462
- Hartmann L., Kenyon S. J., 1996, *ARA&A*, **34**, 207
- Herbig G. H., 1977, *ApJ*, **217**, 693
- Herbig G. H., 1989, in *European Southern Observatory Conference and Workshop Proceedings*. pp 233–246
- Hillenbrand L. A., et al., 2019, *ApJ*, **874**, 82
- Hunter T. R., et al., 2017, *ApJ*, **837**, L29
- Irwin M., 2009, *UKIRT Newsletter*, **25**, 15
- Jackson J. M., Finn S. C., Rathborne J. M., Chambers E. T., Simon R., 2008, *ApJ*, **680**, 349
- Johnstone D., Hendricks B., Herczeg G. J., Bruderer S., 2013, *ApJ*, **765**, 133
- Koenig X. P., Leisawitz D. T., 2014, *ApJ*, **791**, 131
- Lin D. N. C., Papaloizou J., 1985, in Black D. C., Matthews M. S., eds, *Protostars and Planets II*. pp 981–1072
- Lindgren L., et al., 2018, *A&A*, **616**, A2
- López-Corredoira M., Cabrera-Lavers A., Garzón F., Hammersley P. L., 2002, *A&A*, **394**, 883
- Lucas P. W., Roche P. F., 1997, *MNRAS*, **286**, 895
- Lucas P. W., et al., 2017, *MNRAS*, **472**, 2990
- Lucas P. W., et al., 2020, *MNRAS*, **492**, 4847
- Marton G., Tóth L. V., Paladini R., Kun M., Zahorecz S., McGehee P., Kiss C., 2016, *MNRAS*, **458**, 3479
- McClure M., 2009, *ApJ*, **693**, L81
- Meisner A. M., Lang D., Schlafly E. F., Schlegel D. J., 2019, *PASP*, **131**, 124504
- Minniti D., 2016, in *Galactic Surveys: New Results on Formation, Evolution, Structure and Chemical Evolution of the Milky Way*. p. 10
- Minniti D., et al., 2010, *New Astron.*, **15**, 433

- Minniti D., Saito R. K., Alonso-García J., Lucas P. W., Hempel M., 2011, *ApJ*, **733**, L43
- Molinari S., et al., 2010, *PASP*, **122**, 314
- Molinari S., et al., 2016, *A&A*, **591**, A149
- Mróz P., et al., 2015, *Acta Astron.*, **65**, 313
- Peretto N., Fuller G. A., 2009, *A&A*, **505**, 405
- Peretto N., Lenfestey C., Fuller G. A., Traficante A., Molinari S., Thompson M. A., Ward-Thompson D., 2016, *A&A*, **590**, A72
- Planck Collaboration et al., 2016, *A&A*, **594**, A28
- Pokhrel R., et al., 2018, *ApJ*, **853**, 5
- Purcell C. R., et al., 2012, *MNRAS*, **426**, 1972
- Reid M. J., et al., 2019, *ApJ*, **885**, 131
- Rieke G. H., et al., 2004, *ApJS*, **154**, 25
- Robin A. C., Reylé C., Derrière S., Picaud S., 2003, *A&A*, **409**, 523
- Robitaille T. P., Whitney B. A., Indebetouw R., Wood K., 2007, *ApJS*, **169**, 328
- Robitaille T. P., et al., 2008, *AJ*, **136**, 2413
- Romanova M. M., Kulkarni A. K., Lovelace R. V. E., 2008, *ApJ*, **673**, L171
- Safron E. J., et al., 2015, *ApJ*, **800**, L5
- Saito R. K., et al., 2012, *A&A*, **537**, A107
- Schönrich R., Binney J., Dehnen W., 2010, *MNRAS*, **403**, 1829
- Shakura N. I., Sunyaev R. A., 1973, *A&A*, **500**, 33
- Simon R., Rathborne J. M., Shah R. Y., Jackson J. M., Chambers E. T., 2006, *ApJ*, **653**, 1325
- Vasyunina T., Linz H., Henning T., Zinchenko I., Beuther H., Voronkov M., 2011, *A&A*, **527**, A88
- Vorobyov E. I., Basu S., 2006, *ApJ*, **650**, 956
- Vorobyov E. I., Basu S., 2010, *ApJ*, **719**, 1896
- Vorobyov E. I., Basu S., 2015, *ApJ*, **805**, 115
- Ward-Thompson D., Robson E. I., 1990, *MNRAS*, **244**, 458
- Whitaker J. S., Jackson J. M., Rathborne J. M., Foster J. B., Contreras Y., Sanhueza P., Stephens I. W., Longmore S. N., 2017, *AJ*, **154**, 140
- Whitney B. A., Hartmann L., 1993, *ApJ*, **402**, 605
- Wienen M., et al., 2015, *A&A*, **579**, A91
- Wright E. L., et al., 2010, *AJ*, **140**, 1868

of the brightness of central flux peak, for comparison with the earlier data.

This paper has been typeset from a $\text{\TeX}/\text{\LaTeX}$ file prepared by the author.

APPENDIX A: ADDITIONAL PHOTOMETRY

A difficulty with the VVV/VVVx data is that the source was not only saturated at maximum brightness (i.e. in 2010-2013 and in a minority of images from 2014) but also spatially extended on a scale of a few arc seconds, though the flux profile is strongly peaked, see Figure 2. The saturation level varies between the 16 VISTA/VIRCAM arrays. Inspection of the radial intensity profile of the source in VISTA paw-print images from the 4 arrays with detections showed that the profile just outside the saturated core resembles that of a point source. From the photometric apertures provided by the Cambridge Astronomical Survey Unit's VISTA pipeline we used apertures 3 and 4 (diameters of $2''$ and $2\sqrt{2}''$, respectively) to compute a saturation-corrected magnitude in a similar manner to that described by Irwin (2009). This was done for the 2010-2013 data, with an estimated uncertainty of 0.2 mag, and visual comparison with saturated stars having 2MASS photometry was used to check that the results were sensible. Saturated data from 2014 were discarded because the image profile had changed. For unsaturated K_s data from 2014 onward, and for the other VVV passbands, we give point source photometry in aperture 3. This will slightly underestimate the total brightness of the source but it provides a reasonably consistent measurement

Table A1. Additional time series photometry for WISE 1422-6115

Dataset	MJD	Bandpass	Magnitude	Error
DENIS	51014.69	K_s	>13.6	
2MASS	51615.29	K_s	>15.0	
GLIMPSE	53075.39	[3.6]	14.41	0.13
GLIMPSE	53075.56	[4.5]	13.08	0.15
GLIMPSE	53075.39	[5.8]	12.44	0.17
GLIMPSE	53075.56	[8.0]	11.57	0.32
MIPSGAL	53834.33	[24]	4.74	0.03
<i>Akari</i> /IRC	-	[9]	5.90	0.35
<i>Akari</i> /IRC	-	[18]	3.83	0.03
VVV/VVVx	55274.245	Z	>20.0	
VVV/VVVx	55281.254	Y	19.14	0.10
VVV/VVVx	55281.255	Y	19.42	0.15
VVV/VVVx	55282.162	Y	19.44	0.16
VVV/VVVx	55282.163	Y	19.55	0.21
VVV/VVVx	55274.253	J	16.07	0.02
VVV/VVVx	55274.255	J	16.06	0.02
VVV/VVVx	55288.293	J	16.11	0.02
VVV/VVVx	55288.295	J	16.11	0.02
VVV/VVVx	55274.245	H	12.65	0.02
VVV/VVVx	55288.285	H	12.68	0.02
VVV/VVVx	57176.178	H	16.30	0.03
VVV/VVVx	57176.179	H	16.27	0.04
VVV/VVVx	57181.250	H	16.34	0.05
VVV/VVVx	57181.252	H	16.26	0.05
VVV/VVVx	55260.34247	K_s	9.08	0.20
VVV/VVVx	55260.3431	K_s	9.19	0.20
VVV/VVVx	55260.34724	K_s	9.27	0.20
VVV/VVVx	55260.34796	K_s	9.16	0.20
VVV/VVVx	55262.39191	K_s	9.2	0.20
VVV/VVVx	55262.39336	K_s	9.25	0.20
VVV/VVVx	55262.39404	K_s	9.16	0.20
VVV/VVVx	55264.39126	K_s	9.21	0.20
VVV/VVVx	55264.392	K_s	9.26	0.20
VVV/VVVx	55264.39267	K_s	9.23	0.20
VVV/VVVx	55274.24962	K_s	9.18	0.20
VVV/VVVx	55274.36398	K_s	9.05	0.20
VVV/VVVx	55274.3646	K_s	9.16	0.20
VVV/VVVx	55274.36793	K_s	9.18	0.20
VVV/VVVx	55274.36857	K_s	9.17	0.20
VVV/VVVx	55283.24924	K_s	9.08	0.20
VVV/VVVx	55283.25274	K_s	9.23	0.20
VVV/VVVx	55283.25337	K_s	9.1	0.20
VVV/VVVx	55288.28806	K_s	9.22	0.20
VVV/VVVx	55288.28954	K_s	9.07	0.20
VVV/VVVx	55778.06854	K_s	8.52	0.20
VVV/VVVx	55778.07018	K_s	8.62	0.20
VVV/VVVx	55778.07102	K_s	8.54	0.20
VVV/VVVx	55780.07017	K_s	8.68	0.20
VVV/VVVx	55785.99496	K_s	8.72	0.20
VVV/VVVx	55785.99667	K_s	8.76	0.20
VVV/VVVx	55795.02149	K_s	8.56	0.20
VVV/VVVx	55795.02306	K_s	8.72	0.20
VVV/VVVx	55803.98976	K_s	8.34	0.20
VVV/VVVx	55803.99062	K_s	8.39	0.20
VVV/VVVx	55803.99142	K_s	8.53	0.20
VVV/VVVx	55808.99112	K_s	8.27	0.20
VVV/VVVx	55808.99192	K_s	8.27	0.20
VVV/VVVx	55808.99272	K_s	8.35	0.20
VVV/VVVx	55995.18952	K_s	8.64	0.20
VVV/VVVx	55995.19099	K_s	8.73	0.20
VVV/VVVx	55995.19174	K_s	8.69	0.20
VVV/VVVx	56014.27852	K_s	8.59	0.20
VVV/VVVx	56014.28026	K_s	8.96	0.20
VVV/VVVx	56014.28119	K_s	8.6	0.20

Table A1 – continued

Dataset	MJD	Bandpass	Magnitude	Error
VVV/VVVx	56058.30581	K_s	8.72	0.20
VVV/VVVx	56058.30765	K_s	8.82	0.20
VVV/VVVx	56371.21412	K_s	9.02	0.20
VVV/VVVx	56371.21564	K_s	9.1	0.20
VVV/VVVx	56371.21643	K_s	8.85	0.20
VVV/VVVx	56372.20321	K_s	8.88	0.20
VVV/VVVx	56372.20405	K_s	9.01	0.20
VVV/VVVx	56372.20483	K_s	8.93	0.20
VVV/VVVx	56372.20566	K_s	8.91	0.20
VVV/VVVx	56373.19458	K_s	8.99	0.20
VVV/VVVx	56373.19615	K_s	9.04	0.20
VVV/VVVx	56373.19759	K_s	8.89	0.20
VVV/VVVx	56374.19197	K_s	9.06	0.20
VVV/VVVx	56375.25579	K_s	8.59	0.20
VVV/VVVx	56375.2566	K_s	8.61	0.20
VVV/VVVx	56375.25738	K_s	8.65	0.20
VVV/VVVx	56375.25819	K_s	8.47	0.20
VVV/VVVx	56419.25141	K_s	8.57	0.20
VVV/VVVx	56419.25216	K_s	8.7	0.20
VVV/VVVx	56419.25293	K_s	8.76	0.20
VVV/VVVx	56428.3069	K_s	9.06	0.20
VVV/VVVx	56448.22414	K_s	9.08	0.20
VVV/VVVx	56448.22497	K_s	9.14	0.20
VVV/VVVx	56448.22655	K_s	9.1	0.20
VVV/VVVx	56453.21702	K_s	9.02	0.20
VVV/VVVx	56453.21779	K_s	8.85	0.20
VVV/VVVx	56453.21861	K_s	8.92	0.20
VVV/VVVx	56453.2194	K_s	8.78	0.20
VVV/VVVx	56460.99369	K_s	8.91	0.20
VVV/VVVx	56460.99446	K_s	8.99	0.20
VVV/VVVx	56460.99521	K_s	9.12	0.20
VVV/VVVx	56460.99594	K_s	8.91	0.20
VVV/VVVx	56463.17171	K_s	9.21	0.20
VVV/VVVx	56463.17253	K_s	9.24	0.20
VVV/VVVx	56463.17329	K_s	9.15	0.20
VVV/VVVx	56463.17412	K_s	9.1	0.20
VVV/VVVx	56466.18514	K_s	9.16	0.20
VVV/VVVx	56466.18668	K_s	9.23	0.20
VVV/VVVx	56466.18747	K_s	9.14	0.20
VVV/VVVx	56467.16656	K_s	8.96	0.20
VVV/VVVx	56467.1674	K_s	9.05	0.20
VVV/VVVx	56467.16816	K_s	9.09	0.20
VVV/VVVx	56468.16904	K_s	9.07	0.20
VVV/VVVx	56468.16983	K_s	9.18	0.20
VVV/VVVx	56468.17057	K_s	9.17	0.20
VVV/VVVx	56468.17137	K_s	9.05	0.20
VVV/VVVx	56469.12137	K_s	9.1	0.20
VVV/VVVx	56813.04202	K_s	11.03	0.02
VVV/VVVx	56813.04381	K_s	10.94	0.02
VVV/VVVx	56813.05533	K_s	11	0.02
VVV/VVVx	56813.0571	K_s	10.92	0.02
VVV/VVVx	56813.96544	K_s	10.94	0.02
VVV/VVVx	56813.96625	K_s	10.96	0.02
VVV/VVVx	56813.96822	K_s	10.96	0.02
VVV/VVVx	56813.97878	K_s	10.94	0.02
VVV/VVVx	56813.97961	K_s	11.02	0.02
VVV/VVVx	56813.98135	K_s	10.95	0.02
VVV/VVVx	56813.9912	K_s	10.95	0.02
VVV/VVVx	56813.99204	K_s	11.01	0.02
VVV/VVVx	56813.99388	K_s	10.96	0.02
VVV/VVVx	56814.00341	K_s	10.94	0.02
VVV/VVVx	56814.00422	K_s	11	0.02
VVV/VVVx	56814.00643	K_s	10.98	0.02
VVV/VVVx	56814.04191	K_s	10.93	0.02

Table A1 – *continued*

VVV/VVVx	56814.04274	K_s	10.95	0.02
VVV/VVVx	56814.04373	K_s	10.95	0.02
VVV/VVVx	56814.04456	K_s	10.96	0.02
VVV/VVVx	56825.01277	K_s	11	0.02
VVV/VVVx	56825.01364	K_s	11.03	0.02
VVV/VVVx	57118.15631	K_s	12.03	0.02
VVV/VVVx	57118.15709	K_s	12.05	0.02
VVV/VVVx	57134.0828	K_s	12.1	0.02
VVV/VVVx	57150.03191	K_s	12.08	0.02
VVV/VVVx	57150.03299	K_s	12.08	0.02
VVV/VVVx	57150.0339	K_s	12.11	0.02
VVV/VVVx	57150.03507	K_s	12.1	0.02
VVV/VVVx	57165.0114	K_s	12.09	0.02
VVV/VVVx	57165.01219	K_s	12.16	0.02
VVV/VVVx	57165.01362	K_s	12.14	0.02
VVV/VVVx	57165.01452	K_s	12.14	0.02
VVV/VVVx	57171.02674	K_s	12.1	0.02
VVV/VVVx	57171.02757	K_s	12.16	0.02
VVV/VVVx	57171.02829	K_s	12.14	0.02
VVV/VVVx	57171.02911	K_s	12.14	0.02
VVV/VVVx	57172.05397	K_s	12.1	0.02
VVV/VVVx	57172.05474	K_s	12.12	0.02
VVV/VVVx	57172.05543	K_s	12.18	0.02
VVV/VVVx	57172.05623	K_s	12.17	0.02
VVV/VVVx	57176.18236	K_s	12.14	0.02
VVV/VVVx	57176.18403	K_s	12.17	0.02
VVV/VVVx	57181.25722	K_s	12.12	0.02
VVV/VVVx	57585.07992	K_s	12.65	0.02
VVV/VVVx	57585.0807	K_s	12.68	0.02
VVV/VVVx	57585.08142	K_s	12.69	0.02
VVV/VVVx	57585.08222	K_s	12.7	0.02
VVV/VVVx	57928.18046	K_s	13.21	0.02
VVV/VVVx	57933.0333	K_s	13.19	0.02
VVV/VVVx	57933.03393	K_s	13.18	0.02
VVV/VVVx	57933.03461	K_s	13.22	0.02
VVV/VVVx	57933.03533	K_s	13.21	0.02
VVV/VVVx	58208.31044	K_s	13.66	0.02
VVV/VVVx	58208.31118	K_s	13.67	0.02
VVV/VVVx	58212.39832	K_s	13.7	0.03
VVV/VVVx	58262.99078	K_s	13.85	0.02
VVV/VVVx	58262.99156	K_s	13.81	0.02
VVV/VVVx	58654.20043	K_s	14.28	0.03
VVV/VVVx	58654.20121	K_s	14.27	0.03
VVV/VVVx	58654.20198	K_s	14.33	0.03
VVV/VVVx	58654.20271	K_s	14.31	0.03
VVV/VVVx	58701.08159	K_s	14.34	0.02
VVV/VVVx	58701.08231	K_s	14.34	0.02
VVV/VVVx	58701.08303	K_s	14.37	0.02
VVV/VVVx	58701.08378	K_s	14.37	0.03
VVV/VVVx	58702.06429	K_s	14.32	0.03
VVV/VVVx	58702.06503	K_s	14.36	0.02
VVV/VVVx	58702.06659	K_s	14.4	0.02
VVV/VVVx	58702.06742	K_s	14.37	0.03

Table A2. *Herschel*/HiGal and ATLASGAL scaled photometry for HIGALBM 313.6699-0.3092

Wavelength (μm)	Flux (Jy)	Error (Jy)
70	3.12	0.14
160	10.89	0.16
250	14.66	0.41
350	4.48	0.22
500	2.37	0.15
870	0.97	0.19